J Mater Sci (2007) 42:207–214
DOI 10.1007/s10853-006-1053-0

Electron microscopy study of ion beam synthesized β-$FeSi_2$

M. Marinova · E. Sutter · M. Baleva

Received: 24 November 2005 / Accepted: 11 January 2006 / Published online: 17 December 2006
© Springer Science+Business Media, LLC 2006

Abstract β-$FeSi_2$ embedded in a Si matrix was prepared by ion beam synthesis (IBS). Two step implantation, with energies 60 and 20 keV, of two different doses of the iron ions, 5×10^{15} and 5×10^{16} cm^{-1}, was performed. After the implantation, the samples were subjected to rapid thermal annealing (RTA) at 900 °C. The crystal structure of the resulting material was studied using cross-sectional transmission electron microscopy (XTEM), including high-resolution electron microscopy (HREM). The comparison of the XTEM images with the initial iron ions implantation profiles, simulated by SRIM (Stopping and Range of Ions in Matter) demonstrate that the process of IBS, followed by RTA, preserves the initial implantation profile, implying a negligible Fe atoms diffusion velocity in comparison with the one of the chemical reaction between Fe and Si. The XTEM images show that continuous β-$FeSi_2$ layers are fabricated when there is a stoichiometric region in the initial implantation profile. Fe concentration lower than the stoichiometric one in the whole implantation range results in formation of β-$FeSi_2$ nanocrystallites embedded in the Si matrix. The behavior of the absorption coefficient energy dependences, obtained from the optical transmittance and reflectance measurements, reflects the different crystal structures forming in the two types of samples.

M. Marinova (✉) · M. Baleva
Faculty of Physics, Sofia University, 5 J. Boucher Blvd, 1164 Sofia, Bulgaria
e-mail: m_marinova@phys.uni-sofia.bg

E. Sutter
Center for Functional Nanomaterials, Brookhaven National Laboratory, Upton, NY 11973, USA

Introduction

In the last years there has been an increased interest in a new class of semiconducting materials—the metal silicides. Initially the interest was stimulated by the possibility of using the semiconducting β-$FeSi_2$ with an energy gap of 0.80 eV in structures emitting in the range of transparency of silicon and silicon oxide fibers. Other properties that make the semiconducting silicides and β-$FeSi_2$, in particular, potential candidates for applications in micro- and optoelectronics are: (i) their non-toxicity and low cost; (ii) compatibility with well developed Si technology; (iii) nanocrystallites in silicon matrix can be formed by ion-beam synthesis (IBS) and structures with new properties can be created; (iv) promising photoelectric properties—β-$FeSi_2$ has high absorption coefficient (higher than 10^5 cm^{-1} in the whole visible range) and energy gap lower than that of Si (0.80–0.87 eV according to different authors [1–10]), which makes the material suitable for photovoltaic cells [11–14].

$FeSi_2$ exists in two thermodynamically stable phases: tetragonal, metallic α-$FeSi_2$ and orthorhombic, semiconducting β-$FeSi_2$. $FeSi_2$ also has a metastable metallic cubic low temperature γ-$FeSi_2$ phase. Despite the complicated polymorphism proper to the Fe-Si system, the semiconducting β-$FeSi_2$ phase alone can be formed by ion beam synthesis (IBS), followed by a rapid thermal annealing (RTA). The process of IBS is widely employed to fabricate either surface or buried layers of β-$FeSi_2$ grains or precipitates with different sizes, embedded in a silicon matrix [15]. A key advantage of IBS is the profile control of the implanted iron ions that can be achieved by choosing different doses and energies of Fe ions. IBS is typically followed by

additional annealing at elevated temperatures. Prolonged high-temperature annealing ($T_a \leq 900$ °C, annealing time $t_a > 10$ h) is often used in order to assist coarsening and coalescence of the precipitates formed during the process and to improve the crystalline quality of the Si and β-$FeSi_2$ layers. In such a thermal treatment, however, undesirable degradation of the main parameters of Si devices [16] can take place as a result of the Fe diffusion into the Si. To avoid this complication RTA [17] and pulsed ion beam treatment [18] are often preferred. In previous studies we have demonstrated the successful formation of β-$FeSi_2$ alone at implantation doses lower than 1×10^{17} cm^{-2} and subsequent thermal annealing at temperature $T_a = 900$ °C for time $t_a \geq 30$ s [19]. The crystal structure of the samples, produced at $T_a = 900$ °C and $t_a \geq 60$ s, is studied by Grazing incident asymmetric X-ray diffraction (GIAXRD). The GIAXRD patterns reveal polycrystalline structure of the formed β-$FeSi_2$ phase and a dependence of the prevailing crystalline orientation on the sample thickness [20].

In the present work, we use cross-sectional transmission electron microscopy (XTEM) in order to investigate the crystal structure of β-$FeSi_2$ embedded in Si matrix, prepared by IBS and followed by RTA. We present a detailed characterization of the β-$FeSi_2$ phase formed and the β-$FeSi_2$/Si interface. The quality of this interface is crucial in view of the potential application of the β-$FeSi_2$/Si heterojunctions in solar cells. Thus it is important to establish whether the heterojunction is abrupt and whether the heterojunction takes place between certain crystallographic planes. We also evaluate the size of the nanocrystalline precipitates as quantum size effects are expected in the electronic and optical properties of material with nanoscale precipitates.

Experimental

The samples were prepared by IBS, followed by RTA at a pressure of 6.65×10^{-3} Pa. Two-step implantation process was performed on n-type (100) Si wafers with resistivity 4.3–4.5 Ω cm. Each of the two doses of the $^{56}Fe^+$ ions was implanted with two different energies. The data is summarized in Table 1. The $^{56}Fe^+$ implantation profiles were simulated by Stopping and Range of Ions in Matter (SRIM) [21]. The substrates were heated to a temperature of 400 °C by means of the incident ion beam with current density of 10–15 μA/cm^2. Subsequently, the implanted samples were subjected to RTA at $T_a = 900$ °C for different times (Table 1).

The microstructure of the samples was then investigated using XTEM. The XTEM specimens were prepared by tripod polishing, a method particularly suitable for obtaining large, homogeneously thin electron transparent regions. Polishing was followed by brief ion-milling (<10 min) at a sputtering angle of 4° to minimize any structural modifications due to specimen preparation. The samples were examined in a Philips CM200 TEM operating at 200 kV and JEOL JEM 3000F microscope operating at 300 kV. The crystal structure was analyzed using CaRIne Crystallography software [22].

The room temperature reflectance, R, and transmittance, T, spectra were measured in the energy range 0.38–1.20 eV, using CARRY-5E spectrometer. As long as interference fringes are not observed in these spectra and the Si substrate is transparent in this energy region, the spectral dependences of the absorption coefficient $\alpha(E)$ of the β-$FeSi_2$ phase in the samples can be calculated from the relation:

$$T = \frac{(1-R)^2 \exp(-\alpha d)}{(1-R^2)\exp(-2\alpha d)}. \tag{1}$$

Here d can be regarded as an effective thickness of the β-$FeSi_2$ phase.

Results and discussion

XTEM

Overview XTEM images of the microstructure of the samples under investigation produced with doses of implantation $D_2 = 5 \times 10^{16}$ cm^{-2} (s. 9) and $D_1 = 5 \times 10^{15}$ cm^{-2} (s. 5) are shown in Figs. 1 and 2, respectively. The overview images are compared with the $^{56}Fe^+$ implantation profiles, simulated by SRIM. The implantation profiles show that the Fe concentration in the case of D_1 (s. 5) is lower than the β-$FeSi_2$

Table 1 Implantation doses, energies and duration of the rapid thermal annealing, used in the sample preparation

Sample	Implantation dose D (cm^{-2})	Implantation energy E (keV)	Annealing time t_a (s)
5	5×10^{15}	60 and 20	60
9	5×10^{16}	60 and 20	90

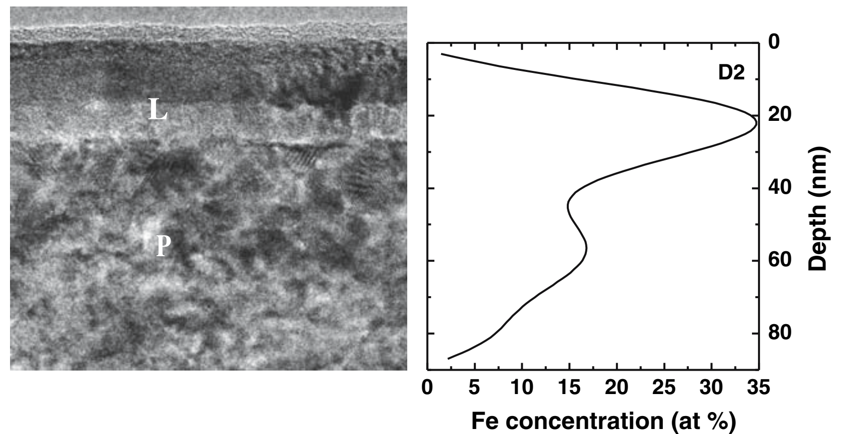

Fig. 1 Overview XTEM image of sample s. 9, prepared with a implantation dose $D_2 = 5 \times 10^{16}$ cm^{-2}. The simulated Fe implantation profile is shown for comparison

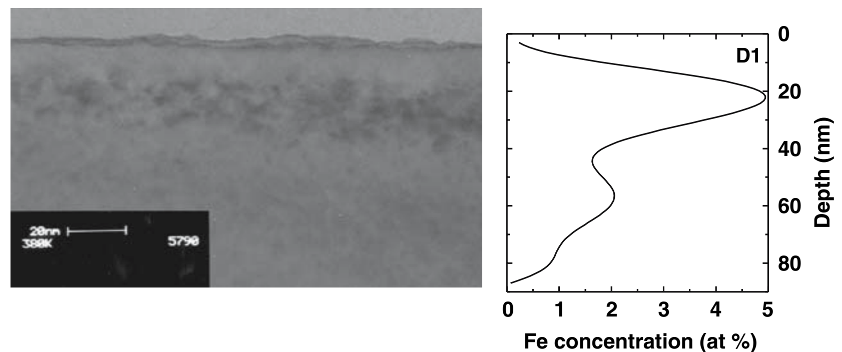

Fig. 2 Overview XTEM image of sample s. 5, prepared with implantation dose $D_1 = 5 \times 10^{15}$ cm^{-2}. The simulated Fe implantation profile is shown for comparison

stoichiometric one over the entire implantation range while in the case of D_2 (s. 9) there is a narrow stoichiometric region close to the surface [21]. It is worth mentioning the good correlation between the observed structure and the simulated concentration profiles. Having into account that the chemical reaction velocity depends on the temperature, one may conclude that at $T_a = 900$ °C the reaction velocity prevails the Fe diffusion one.

The XTEM overview image of s. 9 with Fe concentration higher than the stoichiometric one (Fig. 1) shows the formation of a relatively thin but nevertheless continuous β-$FeSi_2$ layer (L). This layer is polycrystalline and its thickness is about 40 nm. In depth (away from the Si surface) the layer is followed by a region (P) with thickness of about 80–90 nm, representing Si with β-$FeSi_2$ precipitates embedded in it. The Moire fringes, seen in Fig. 1, indicate an overlap of neighbour domains of different orientation or of domains with certain β-$FeSi_2$ phase orientation with the Si lattice.

The XTEM overview image of s. 5 with Fe concentration lower than the stoichiometric one in the whole range of implantation (Fig. 2) shows the formation of the β-$FeSi_2$ phase in the form of precipitates only. The thickness of the quasi-homogeneous layer, representing β-$FeSi_2$ precipitates, embedded in the Si matrix, is evaluated to be about 45 nm.

The microstructure of the samples was further investigated in more detail at higher magnifications in order to identify the growth directions of the different crystalline grains, constituting the polycrystalline layer, and the precipitates as well as to evaluate their sizes.

A typical high resolution XTEM (HREM) image of the continuous polycrystalline layer is given in Fig. 3. The image is from a region, approximately 25 nm below the sample surface. Crystalline domains with different orientations, denoted with A, B, C, and D, are clearly resolved. As a rule the crystalline grains are with prolonged shape. The domains have two characteristic sizes: smaller ones, ~10–14 nm, and larger with sizes exceeding the film thickness. Details of the interfaces between these oriented domains and the Si matrix are given in Figs. 4–6. The interfaces appear to be sharp and no defect regions are observed. The heterojunctions are formed between different β-$FeSi_2$ and Si crystallographic planes. By definition a heterojunction is abrupt when the junction region is of the

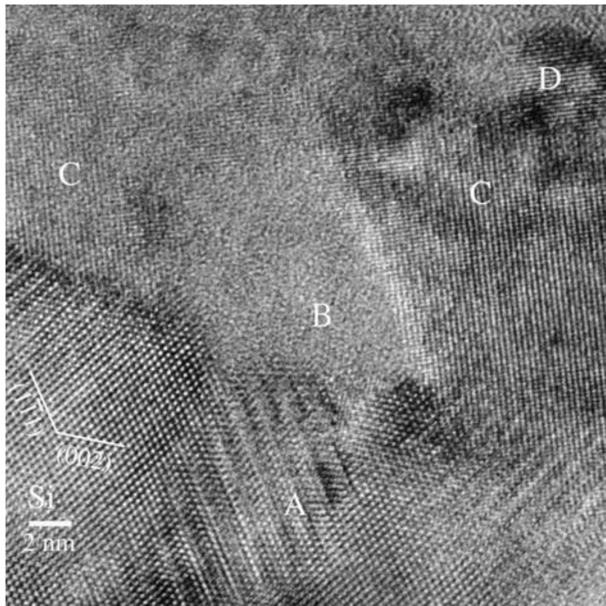

Fig. 3 High-resolution XTEM image from the region of the continuous polycrystalline β-$FeSi_2$ layer is s. 9. The image is from the region L, ~25 nm below the sample surface (Fig. 1)

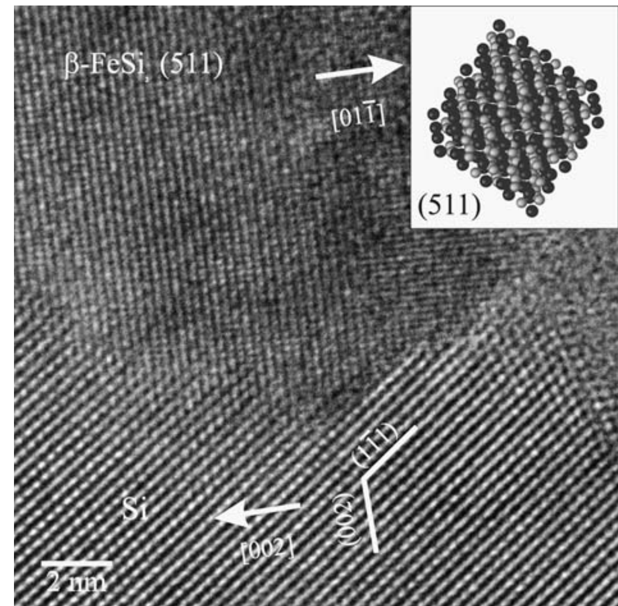

Fig. 5 High-resolution XTEM image, showing an interface between the [01$\bar{1}$] direction of the (511) β-$FeSi_2$ plane and the [002] direction of the (110)Si plane. In the insert the simulated projection of two β-$FeSi_2$ unit cells in [511] directions is given

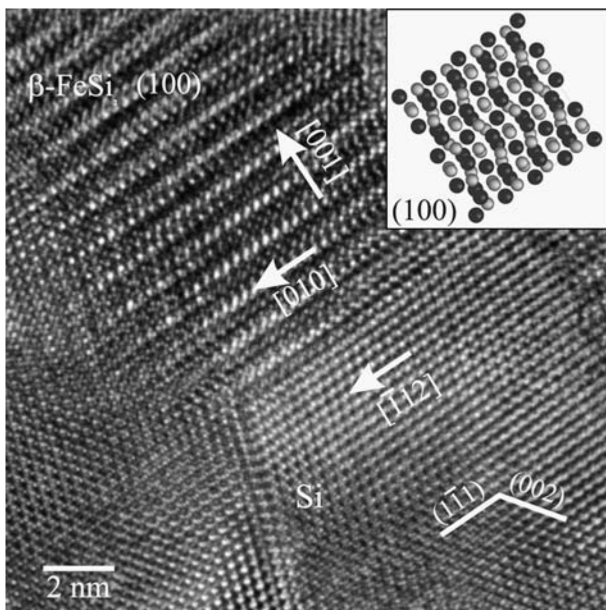

Fig. 4 High-resolution XTEM image, showing an interface between the [010] direction of the (100) β-$FeSi_2$ plane and the [$\bar{1}$12] direction of the (110) Si plane. In the insert the simulated projection of two β-$FeSi_2$ unit cells in [100] direction is given

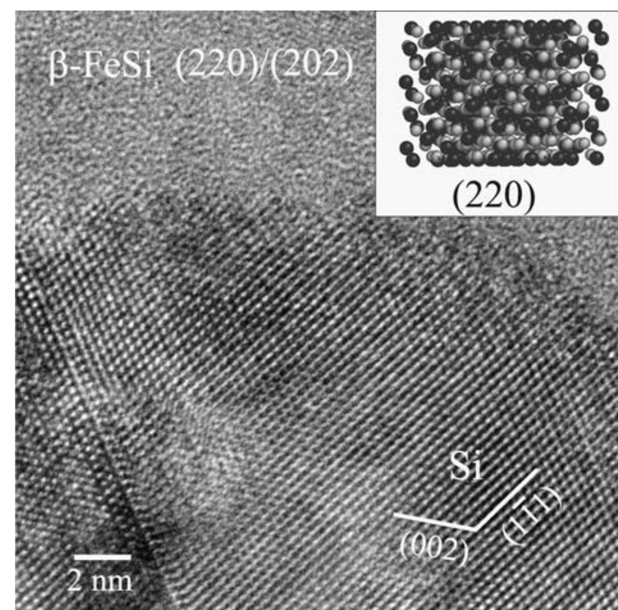

Fig. 6 High-resolution XTEM image, showing an interface between the (220)/(202) β-$FeSi_2$ plane and the (110) Si plane. In the insert the simulated projection of two β-$FeSi_2$ unit cells in [220] direction is given

order of several interatomic distances. It can be seen that independent of the type of the contacting planes, the formed β-$FeSi_2$/Si heterojunctions in sample s. 9 can be characterized as abrupt ones. It is seen that despite of their abruptness the hetejunctions are only flat in the region of a grain. On macroscopic scale heterojunction interface is not parallel to the Si surface. This results in a junction area much larger

than in the case of a flat interface, a feature expected to be advantageous for solar cell applications. The same kind of heterojunctions, not straightforward, but with clear interfaces, are observed by Meada et al. [13] in the overview pictures of samples, implanted with the same dose and subjected to conventional annealing at 800 °C for longer time.

The insets in Figs. 4–6 show β-$FeSi_2$ structural simulations performed using the CaRIne Crystallography v.3.1 software [22]. Based on the structure simulations the following β-$FeSi_2$ phase planes were identified in the different domains—(100) in the A domain; (202)/(220) in the B domain; (511) in the C domain; and (422) in the D domain. The simulated projections of two β-$FeSi_2$ unit cells in [100], [511] and [220] directions are given in the insets of Figs. 4–6, respectively.

As it is seen from Figs. 1 and 3, the distribution of the domains with different orientation is not uniform along the layer thickness. In the region, where the Fe concentration exceeds the stoichiometric one, mainly domains, orientated in [202]/[220] direction—the B domains (these two directions can hardly be resolved because of the close values of the lattice parameters on the c and b axis), are observed. C domains with [511] orientation are randomly distributed over the continuous layer and the regions with nanocrystallites. Domains with [100] orientation (A domains) are observed only at the β-$FeSi_2$/Si interface. It should be pointed out that the {511} planes (C domains) and the {100} planes (A domains) are rotated with respect to one another at a small angle, 12.63°, around the [001] direction. One can then speculate that the Fe-deficiency favors the orientation relations (100) β-$FeSi_2$// (110) Si with [010] β-$FeSi_2$//[$\bar{1}$12] Si and (511) β-$FeSi_2$ //(110) Si with [$\bar{1}$01] β-$FeSi_2$//[002] Si, as denoted in Figs. 4 and 5. The same wavy contrast, as the one shown in Fig. 4, which indicates (100) β-$FeSi_2$ orientation, is observed by Shao et al. [15] in β-$FeSi_2$ precipitates, produced by IBS with iron ions dose 2×10^{16} cm^{-2} and implanted at much higher energy (950 keV). A HREM image, taken from a region, lying deeper, at about 50 nm below the surface of s. 9, is given in Fig. 7. Randomly distributed β-$FeSi_2$ precipitates, oriented into [511] direction relative to the (110) Si plane, alone can be observed in the region. The sizes of these precipitates are evaluated to vary from 4 to 8 nm. An enlarged structure of the β-$FeSi_2$ precipitates is also given in Fig. 7.

The crystal structure of s. 9 was compared to the GIAXRD study of the crystal structure of a sample, produced at the same implantation regime as s. 9, but annealed for a shorter time (60 s) at the same annealing temperature. The GIAXRD patterns, taken at grazing angles 5°, 7°, and 15° are reproduced in Fig. 8 [20]. In the same figure the diffraction spectrum of polycrystalline β-$FeSi_2$ with intensities and positions, taken from PDF database [23], are shown with solid lines below the experimental spectra. Along the most intense (202), (220) reflections the (511), (422) and (411) reflections of the β-$FeSi_2$ phase are detected. The (202), (220) reflections are most intense at grazing angle 7° and decrease at further increase of the angle as the probed film thickness increases. The amount of the (202), (220) β-$FeSi_2$ phase in the middle of the layer is then obviously the largest. The behavior of the reflection intensity coincides fairly well with the TEM observation of s. 9. As it is seen from Fig. 1, β-$FeSi_2$ phase, orientated in [202]/[220] directions forms nearly continuous layer with a thickness of about 10 nm, placed in the middle of the entire area containing β-$FeSi_2$. Similar to the TEM observations, the (511) reflection is with the highest intensity and the (422) reflection is well resolved. The lattice constants a, b and c of the β-$FeSi_2$ phase are calculated from the diffraction pattern shown in Fig. 8. In Table 2 the lattice parameters are compared with the experimental and calculated values a_0, b_0 and c_0 for bulk unstrained β-$FeSi_2$ [24]. Using the experimental lattice constants from Ref. [24] as a reference, the strains ε_a, ε_b and ε_c along the crystal axes ($\varepsilon_a = (a - a_0)/a_0$, $\varepsilon_b = (b - b_0)/b_0$, $\varepsilon_c = (c - c_0)/c_0$) are calculated and given

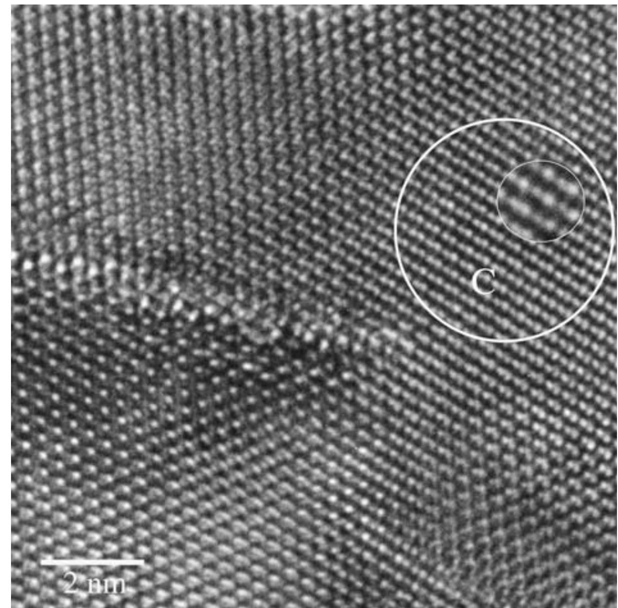

Fig. 7 A typical HREM image from a region ~50 nm below the surface of s. 9, showing randomly distributed 4–8 nm β-$FeSi_2$ precipitates (C domains). The inset shows a detail of the structure

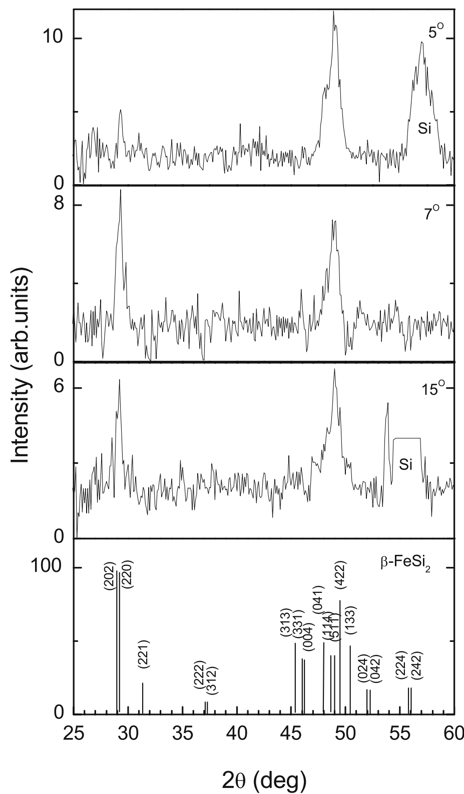

Fig. 8 GIAXRD patterns of a sample, produced at the same implantation regime as s. 9, but annealed for a shorter time (60 s) at the same temperature 900 °C, taken at grazing angles 5°, 7°, and 15°

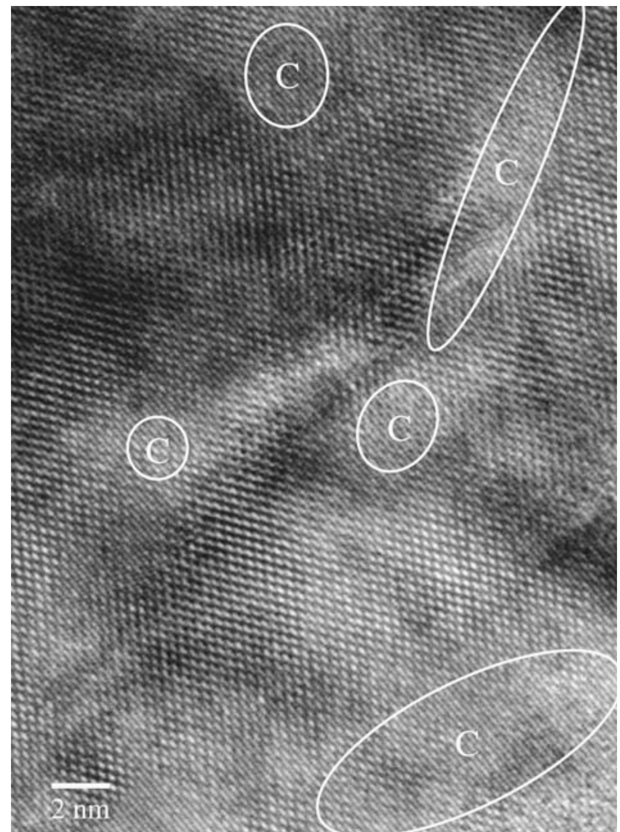

Fig. 9 A typical HREM image of s. 5 with identified nanocrystalline precipitates (C domains)

in Table 2. It is seen that the lattice parameters of the phase, produced by IBS do not differ significantly from those of the bulk phase.

The HREM images of s. 5 reveal only randomly distributed in the Si matrix low dimensional β-$FeSi_2$ nanocrystallites of irregular shape. The nanocrystallites are not uniformly distributed and have two characteristic sizes: smaller one—from 2 to 7 nm, and larger—reaching and even exceeding the thickness of the layer where they can be found. From the HREM image of s. 5, shown in Fig. 9, it is seen that the nanocrystallites in s. 5 have the same crystal orientation as that of the precipitates in the region of s. 9, laying under the continuous polycristalline β-$FeSi_2$ layer. The nanocrystallites crystallize in [511] direction relatively to the (110) Si plane too.

Absorption coefficient dispersions

The dispersions $\alpha(E)d$ for s. 9 and s. 5, as obtained from equation (1), are shown in Fig. 10. A strong absorption at 0.43 eV, a noticeable absorption increase at about 0.60 eV, and a sharp absorption increase at 1.03 eV can be seen in the spectra of both samples. In addition in s. 9 a significant increase in absorption is observed at about 0.80 eV. In the $\alpha(E)d$ dependence of s. 5 an absorption increase, though less pronounced, starts at about 0.90 eV.

Table 2 Lattice parameters of the β-$FeSi_2$ phase in the sample, produced with the same implantation dose as s. 9 and annealed at the same temperature, but for a shorter time (60 s)

Grazing angle	a (Å)	b (Å)	c (Å)	ε_a (%)	ε_b (%)	ε_c (%)
5°	9.881	7.788	7.818	+0.2	–0.0	–0.2
7°	9.894	7.786	7.840	+0.3	–0.1	0.1
Bulk β-$FeSi_2$ [24]	9.863	7.791	7.833			

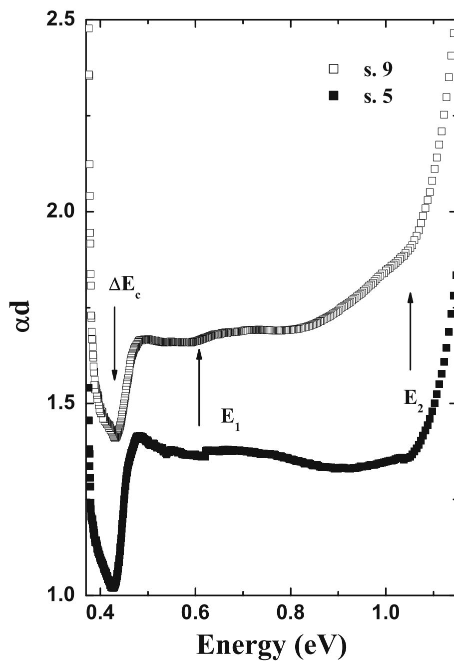

Fig. 10 The energy dependences of the absorption coefficient of samples, prepared with different implantation doses

The $\alpha(E)d$ dependences are shown in the range of transparency of Si. In this region two types of transitions contribute to the absorption—those at the interface between β-$FeSi_2$ and Si, and those in the β-$FeSi_2$ volume.

In the samples under investigation, with large junction area, we expect interface absorption to be significant compared to absorption in the β-$FeSi_2$ phase volume. Then it is reasonable to attribute absorption at 0.43 eV and 1.03 eV to transitions, taking place at the heterojunction. The strong absorption at about 0.43 eV can be attributed to presence of a local electric field at β-$FeSi_2$/Si boundaries and the energy 0.43 eV than gives the β-$FeSi_2$ and Si conduction bands offset. A transition with energy 1.01 ± 0.04 eV is reported to take place at the β-$FeSi_2$/Si interface [11–14]. According to the energy band diagram of β-$FeSi_2$/Si heterojunction, proposed by the Lefki et al. [11] and Muret et al. [12] and confirmed by Okajima et al. [14], two transitions, one with energy $E_1 = 0.60 \pm 0.04$ eV and another with $E_2 = 1.01 \pm 0.04$ eV, govern the photoconductivity spectral dependence of this heterojunction. The transition with $E_1 = 0.60 \pm 0.04$ eV takes place from a trap level, pinning the Fermi level in the β-$FeSi_2$ forbidden gap. The second one, with a larger energy $E_2 = 1.01 \pm 0.04$ eV, is from the same trap level to the Si conduction band (c.b) bottom. at the interface. We believe that the Fermi level is not pinned by a trap level in the β-$FeSi_2$ band gap, but rather by the β-$FeSi_2$ valence band (v.b.) top at the Λ-point of the Brillouin zone with a heavy carrier effective mass. The transition with energy $E_1 = 0.60 \pm 0.02$ eV has better to be attributed to a superposition of indirect transitions from the v.b. top at the Λ-point [1]. The transition with energy E_2, in our case $E_2 \approx 1.03$ eV, then has to take place from the v.b. top to the Si c.b. at the interface. The difference between the energies of these two transitions gives the energy of the c.b. offset at the heterojunction interface — $\Delta E_c = E_{ci}(\text{Si}) - E_{ci}(\beta\text{-FeSi}_2)$, which in our case is 0.43 eV. The width of the absorption band at 0.43 eV as it is seen from Fig. 10 is comparatively broad. This is not surprising if one takes into account that the electron affinity, which determines the c.b. offset at a heterojunction, is different for the different crystallographic planes. Heterojunctions between different crystallographic planes are observed in the HREM images (Fig. 4, 6).

As it can be expected the β-$FeSi_2$ volume absorption is well seen in s. 9, prepared with the higher implantation dose and with a continuous layer formed. In a previous study of thicker β-$FeSi_2$/Si layers, direct energy gap of 0.80 eV is reported [9]. A number of direct and indirect transitions is theoretically predicted [1–8] and experimentally proved [1, 7, 9, 10] in the vicinity of the β-$FeSi_2$ band gap. Thus the absorption coefficient increase in the range from 0.80 to 1.03 eV is due to a superposition of all these transitions. The low absorption in s. 5 in the vicinity of the β-$FeSi_2$ band edge and the high-energy shift apart from the smaller β-$FeSi_2$ amount (lower effective layer thickness) can be related also to a quantization of the energy levels.

Conclusions

The investigation of the cross-sectional morphology of samples, representing Si matrix with iron ions, implanted in it by IBS, lead to the following conclusions: (i) The desired semiconducting β-$FeSi_2$ phase alone is formed at the chosen preparation conditions; (ii) At annealing temperature $T_a = 900$ °C the distribution of the β-$FeSi_2$ phase follows the initial implantation profile of the iron ions indicating negligible diffusion velocity of Fe in comparison with the one of the chemical reaction of β-$FeSi_2$ formation; (iii) The presence of a stoichiometric region in the implantation profile leads to the formation of a well-defined continuous polycrystalline β-$FeSi_2$ layer. Fe concentration lower than the $FeSi_2$ compound stoichiometric one in the whole implantation range results in formation of β-$FeSi_2$ nanocrystallites. The dominant crystal orientation in the polycrystalline layer is [202]/[220] with

respect to the (110) silicon plane in the region where the Fe concentration is comparable with the stoichiometric one and [511] direction predominantly in the Fe deficient region. The crystal orientation of the precipitates in both samples is as that of the grains in the Fe deficient region - they crystallize into [511] direction with respect to the (110) Si plane. The HREM study shows that the β-$FeSi_2$/Si heterojunction, though not flat, is abrupt. Heterojunctions between different crystallographic planes are observed. Nanocrystallites with sizes as low as 2 nm are observed and therefore, the absorption is possibly influenced by quantum size effect.

Acknowledgements The authors are indebted to E. Goranova for supplying the samples and stimulating the interest in this work. The work is supported by the National Fund for Scientific Investigations under contract no. Φ1301/03. The research was performed in part under the auspices of the U.S. Department of Energy, under contract No. DE-AC02-98CH10886.

References

1. Filonov AB, Migas DB, Shaposhnikov VL, Dorozhkin NN, Petrov GV, Borisenko VE, Henrion W, Lange H (1996) J Appl Phys 79:7708
2. Clark SJ, Al-allak HM, Brand S, Abraham RA (1998) Phys Rev B58:10389
3. Miglio L, Meregalli V (1998) J Vac Sci Technol B16:1604
4. Moroni EG, Wolf W, Hafner J, Podloucky R (1999) Phys Rev B59:12860
5. Migas DB, Miglio L (2000) Phys Rev B62:11063
6. Migas DB, Miglio L, Henrion W, Rebien M, Marabelli F, Cook BA, Shaposhnikov VL, Borisenko VE (2001) Phys Rev B64:075208
7. Boast M, Mahn J (1985) J Appl Phys 58:2696
8. Lefki K, Muret P, Cherief N, Cinti RC (1991) J Appl Phys 69:352
9. BalevaV, Surtchev M, Goranova E (2000) Phys Rev B62: 13057
10. Darakchieva V, Baleva M, Goranova E, Angelov CH (2000) Vacuum 58: 415
11. Lefki K, Muret P (1993) Appl Surf Sci 65/66: 772
12. Muret P, Lefki K, Nguen TTA, Cola A, Ali I (1994) Semicond Sci. Technol. 9: 1395
13. Maeda Y, Umezawa K, Hayashi Y, Miyake K, Ohashi K (2001) Thin Solid Films 381: 256
14. Okajima K, Yamatsugu H, Wen C, Sudoh M, Yamada K (2001) Thin Solid Films 381: 262
15. Shao G, Homewood KP (2000) Intermetalics 8: 1405
16. Kolbesen BO, Serva H (2000) Phys Stat Sol B222: 303
17. Behar M, Bernas H, Desimoni J, Lin XW, Maltez RL (1996) Appl Phys 75: 752
18. Batalov RI, Bayazitov RM, Khaibullin JB, Terukov EI, Kh. Kudoyarova VKh (2001) Nanotechnology 12: 409
19. Darakchieva V, Surtchev M, Goranova E, Baleva M (2003) Vacuum 60: 449
20. Atanassov A, Baleva M, Goranova E, Darakchieva V (2004) Vacuum 76: 277
21. Baleva M, Goranova E, Angelov Ch, Beshkov G (2003) J Mat Sci Electr 14: 849
22. CaRIne Crystallography v.3.1 software, © 1989-1998 C. BOUDIAS & D. MONCEAU, Divergent S. A. Centre de Trandfert 60200 Compiegne France
23. PDF database (1997) ICPDS International Center for Diffraction Data
24. Dusausoy Y, Protas J, Wandji R, Roques B (1971) Acta Cryst B27:1209